# Conduction via surface states in antiferromagnetic Mott-insulating $NiS_2$ single crystals

Sami El-Khatib,[1,2] Bryan Voigt,[2] Bhaskar Das,[2] Axel Stahl,[2] William Moore,[2] Moumita Maiti,[2] and Chris Leighton[2,*]

[1]*Department of Physics, American University of Sharjah, Sharjah, United Arab Emirates*

[2]*Department of Chemical Engineering and Materials Science, University of Minnesota, Minneapolis, Minnesota 55455, USA*

(Received 10 September 2021; accepted 11 November 2021; published 23 November 2021)

Pyrite structure transition-metal disulfides exhibit diverse ground states vs $d$-band filling, spanning diamagnetic semiconducting, ferromagnetic metallic, antiferromagnetic Mott insulating, and superconducting in $FeS_2$, $CoS_2$, $NiS_2$, and $CuS_2$. $NiS_2$ is particularly interesting and poorly understood as its Mott insulating behavior is accompanied by complex antiferromagnetic ordering below ~38 K and perplexing weak ferromagnetism below ~30 K. Temperature-, pressure-, and composition-dependent insulator-metal transitions also occur, particularly in bandwidth-controlled $NiS_{2-x}Se_x$, hole-doped $Ni_{1-x}Co_xS_2$, etc. Here, we use high-quality chemical-vapor-transport-grown $NiS_2$ single crystals characterized by x-ray diffraction, energy-dispersive x-ray spectroscopy, magnetometry, and extensive transport and magnetotransport measurements, to generate new insight into this system. In particular, resistivity, magnetoresistance, and Hall effect analyses vs temperature, thickness, and surface preparation, provide unequivocal evidence of surface conduction, where the more conductive surface shunts essentially all current at low temperatures. The surface transport changes from two dimensional and insulating to three dimensional and metallic as the surface preparation is varied (also displaying intriguing sensitivity to magnetic ordering), significantly clarifying literature ambiguities with respect to the electronic ground state. These results have immediate implications. First, the temperature-, pressure-, and composition-dependent insulator-metal transitions deduced in the extensive prior work on $NiS_{2-x}Se_x$, $Ni_{1-x}Co_xS_2$, etc., must clearly be reexamined in light of rife metallic surface conduction, not previously taken into account. Second, $NiS_2$ now joins $FeS_2$ and $CoS_2$ as systems in which bulk and surface electronic behaviors are strikingly different, suggesting that metallic surface states could be a universal feature of pyrite structure transition-metal disulfides.

DOI: 10.1103/PhysRevMaterials.5.115003

## I. INTRODUCTION

The pyrite structure transition-metal (TM) disulfides are a remarkable, arguably underexplored, family of compounds [1–4]. From $MnS_2$ through $ZnS_2$ their $d$-band filling varies while maintaining the relatively simple pyrite structure (space group $Pa\bar{3}$), wherein a face-centered-cubic (fcc) sublattice of $TM^{2+}$ ions interpenetrates an fcc $(S_2)^{2-}$ dimer array [1–4]. The resulting diversity in electronic and magnetic behaviors is striking, encompassing a spin-state crossover compound ($MnS_2$), a diamagnetic semiconductor of interest for photovoltaic (among other) applications ($FeS_2$), a ferromagnetic (FM) metal ($CoS_2$), an antiferromagnetic (AFM) Mott insulator ($NiS_2$), a superconductor ($CuS_2$), and a wide band-gap semiconductor ($ZnS_2$) [1–4]. Ternary $TMS_2$ solid solutions provide further control over band filling and properties, including tunable spin polarization in F $Co_{1-x}Fe_xS_2$ [5–8], and FM/AFM phase competition and metamagnetism in $Co_{1-x}Ni_xS_2$ [1–4]. *Voltage-based* control of transport and magnetism has also been demonstrated in electrolyte-gated $FeS_2$ [9].

$NiS_2$ is a particularly prominent and challenging member of the pyrite $TMS_2$ family. The $Ni^{2+}$ ($d^8$) nominal $t_{2g}{}^6e_g{}^2$ electronic configuration in this system is thought to lead to a Mott insulating ground state with a small energy gap [1–4,10–21]. In terms of magnetism, AFM order occurs below a Néel temperature ($T_N$) of ~39 K [11,12,14,15,18–21], albeit with a complex noncollinear spin structure [11,14,15,18,20], likely related to the frustration inherent to antiferromagnetically interacting spins on the fcc Ni sublattice. Weak ferromagnetic (FM) behavior then emerges below $T_{wf} \approx 30$K [11,12,14,15,18–21]. The latter is perplexing and as yet unexplained, as weak FM is nominally forbidden in this crystal/magnetic structure [20]. Several studies thus examined potential structural distortions accompanying the magnetic transitions in $NiS_2$, but with no clear consensus [14,18,20]. The transition at $T_{wf}$ is also apparently first order, but with thermal hysteresis of only ~0.1 K [12]. Even the magnetic behavior above $T_N$ presents challenges in $NiS_2$. Clear deviations from Curie-Weiss (C-W) susceptibility occur, which have been interpreted either in terms of frustration (the frustration ratio $\theta_{CW}/T_N$, where $\theta_{CW}$ is the C-W temperature, has been reported to be as high as ~30) [15], or an unexplained surface contribution [14].

Remarkably, electronic transport in this system is perhaps even richer. The high-temperature (~100–300 K) resistivity ($\rho$) takes a simple Arrhenius form, with activation energy in the 70–120-meV range [15,19,21], which has been claimed to be consistent with the known electronic structure [21]. The Hall effect in this regime is small [13] and nontrivial to interpret in such a Mott insulator, as is the lower-$T$ transport behavior. In particular, below ~100 K a distinct change in $\rho(T)$ occurs to a much weaker $T$ dependence, the details

*leighton@umn.edu

 

of which are widely variable [13,15,16,19–23]. Metalliclike behavior (positive $d\rho/dT$), insulatinglike behavior (negative $d\rho/dT$), and crossovers between the two have all been reported on cooling [13,15,16,19–23], leading to uncertainty over the true electronic ground state. This complexity is only amplified with chemical substitution and/or application of hydrostatic pressure. Both electron and hole doping are possible, in $Ni_{1-x}Cu_xS_2$ and $Ni_{1-x}Co_xS_2$, respectively, leading to an electron/hole-asymmetric insulator-metal transition (IMT) by $x \approx 0.1$ [1–4,24–26]. This is accompanied by complex (in some cases nonmonotonic) doping-induced evolutions of $T_N$ and $T_{wf}$, which are again poorly understood [3,4]. The most heavily studied chemical substitution, however, is the isovalent one in $NiS_{2-x}Se_x$, where a bandwidth-controlled Mott-Hubbard IMT is thought to occur [3,4,22,23,27]. The evolution of the transport behavior with $x$ and pressure in $NiS_{2-x}Se_x$ is rich, crossing over from the abovementioned flattening of $\rho(T)$ at low $T$, to a regime with a prominent low-$T$ peak in $\rho(T)$, to a metallic state with indications of unconventional $T$ dependence [3,4,17,22,23,27]. Just as for the magnetic properties, many features of the electronic transport in $NiS_2$ thus require substantial further elucidation.

Critically, many of the above transport studies were conducted from the 1970s to 1990s [1–4,10,17,22–27]. In 1994, however, Thio and Bennett [13] arrived at a remarkable conclusion by analyzing $T$-dependent resistivity and Hall effect data on $NiS_2$, deducing a vital role for *surface conduction*. Specifically, they concluded that the flattening of $\rho(T)$ at low $T$ occurs due to current shunting by a metallic surface layer in typical (horizontal) transport measurements, which they captured via simple two-channel (i.e., surface and bulk) conduction modeling [13]. The metallic surface was found to have two-dimensional (2D) hole density $\sim 5 \times 10^{14}$ cm$^{-2}$ . While several scenarios were discussed, no firm conclusions were reached regarding the origin of this surface conduction [13]. Importantly, this insight was reached *after* the publication of much of the work on $NiS_2$ IMTs vs electron/hole doping, Se substitution, and pressure [1–4,10,23–27], and seems to have been fully acknowledged in only a few subsequent works (e.g., Refs. [14,16,21,28]). Photoemission spectroscopy was later performed, however, confirming the metallic nature of the surface, along with unusual $T$-dependent variations in the surface density of states at the Fermi level ($E_F$), which correlate with $\rho(T)$ [16]. Studies of nanocrystalline $NiS_2$ have also uncovered evidence for metallic surface conduction [29].

More recently, the importance of surface phenomena in *other* pyrite structure $TMS_2$ compounds has become progressively apparent. Most notably, the diamagnetic semiconductor $FeS_2$ ($t_{2g}{}^6e_g{}^0$ electronic configuration) has been unequivocally demonstrated to exhibit surface conduction [30,31]. In that case a higher-conductivity $p$-type inverted surface layer forms spontaneously on $n$-type crystals [30–32] (which are typically unintentionally doped with S vacancies [33,34]), as verified by extensive transport and magnetotransport observations and analyses [30,31,35]. The transport observations include flattening of $\rho(T)$ at low $T$ due to surface shunting [30,31,35], thickness-dependent $\rho$ in this regime [30,31,35], sensitivity to surface preparation [30,31], 2D character to the low-$T$ transport [31], and a systematic $n - p$ crossover in the Hall effect [31], all of which are captured by two-channel (surface and bulk) modeling [30,31,35]. Such findings correlate well with earlier photoemission spectroscopy observations of surface $E_F$ pinned near the valence-band edge in $FeS_2$ [36–39], providing a consistent interpretation. Surface states intrinsic to the $FeS_2$ surface have been touted as the likely origin of these effects [30–32,35–39]. Recent work has clarified the resulting surface band bending [30–32,35,37], its implications for performance of $FeS_2$-based solar cells [30–32,35,37], and even routes to mitigation of surface conduction, thereby accessing bulk low-$T$ transport [40]. Perhaps less widely acknowledged, but no less relevant, the efforts to realize half-metallic ferromagnetism (i.e., 100% spin polarization at $E_F$) in the filling-tuned $Co_{1-x}Fe_xS_2$ system [5–8] were likely thwarted by another surface effect [41]. While high spin polarization (up to 85%) was achieved in $Co_{1-x}Fe_xS_2$ [6–8], minority spin surface states were directly observed [41], likely preventing a half-metallic ground state in $Co_{1-x}Fe_xS_2$. Most recently it was pointed out that topologically nontrivial features (specifically Weyl cones) arise in the band structure of $CoS_2$, not far from $E_F$ [42], not only stimulating renewed interest in these systems, but also highlighting further possible routes to surface conduction phenomena.

Taken together, these observations, particularly the recent developments, indicate that $NiS_2$ is surely now ripe for additional study and reexamination, particularly with respect to key questions regarding surface effects. First, it would clearly be of high interest to more rigorously establish surface conduction in $NiS_2$, particularly in the highest-quality single crystals available, and particularly using the various transport measurements and analyses that proved so successful in recent studies of $FeS_2$. Second, it is imperative to establish to what extent the existence of surface conduction could bring into question, or even invalidate, earlier conclusions from the large body of work on the IMT in doped, substituted, and pressurized $NiS_2$. Finally, with evidence accumulating that surface phenomena play a prominent role in the properties of several $TMS_2$ compounds, it also becomes important to understand if surface states could be a generic feature of these materials, with broad potential implications. The origin of such surface states would then become a key question.

In the above context, in this work we revisit electronic transport and magnetism in $NiS_2$, using thoroughly characterized, high-quality, chemical vapor transport (CVT) single crystals. The magnetic properties are found to be in close accord with earlier work, including an ~38 K Néel temperature and ~29 K onset of weak ferromagnetism. A series of transport and magnetotransport measurements and analyses are then used to compile unequivocal evidence of surface conduction. Abrupt flattening of $\rho(T)$ due to surface shunting at low $T$, thickness-dependent $\rho$, sensitivity to surface treatment, and consistency with two-channel (bulk and surface) conduction modeling are all demonstrated. The low-$T$ surface ground state is found to be remarkably variable, from 2D and insulating in pristine as-grown crystals (with conduction *via* Efros-Shklovskii variable-range hopping), to 3D and metallic (weakly localized) in polished crystals, with intriguing sensitivity of the resistivity to magnetic ordering. $T$-dependent measurements of the Hall effect and magnetoresistance (MR) are then found to be in good agreement with these deductions. Overall, these findings put surface conduction on a firm

footing in $NiS_2$, provide substantial insight into scattered prior literature deductions regarding the electronic ground state, and establish this compound as another example of a $TMS_2$ system profoundly impacted by surface effects. We thus hypothesize that surface states could be a universal feature of $TMS_2$ compounds, with broad potential implications.

## II. EXPERIMENT DETAILS

$NiS_2$ single crystals were grown via the CVT method, as previously applied to various $TMS_2$ compounds (e.g., Refs. [2,3,10–17,24–27,31,33,35,40,42,43]). Precursor powders of Ni (Alfa Aesar, 99.999% purity), S (CERAC, 99.9995% purity), and $NiBr_2$ (Sigma-Aldrich, 99.999% purity) were placed in evacuated ($\sim 10^{-6}$ Torr), sealed quartz ampoules. Crystal growth then proceeded for 16 d in a two-zone tube furnace with hot and cold-zone temperatures of 700 and 650 °C; as in our prior work [31,33,35,40,43], the hot and cold zones were inverted for 3 d at the beginning of the growth. After growth, the crystals were cleaned in solvent to remove any residual S and $NiBr_2$. Powder x-ray diffraction (XRD) was performed on ground crystals in a Rigaku MiniFlex system with a graphite monochromator, using Cu $K_\alpha$ x-rays. Lattice parameters were determined via the sample height offset correction method. High-resolution XRD was done in a Panalytical X'Pert Pro diffractometer, again using Cu $K_\alpha$. Energy-dispersive x-ray spectroscopy (EDS) was also performed, in a JEOL 6500F field-emission scanning electron microscope equipped with a Thermo-Noran Vantage EDS system.

Magnetometry measurements were made in a Quantum Design superconducting quantum interference device magnetometer (Magnetic Property Measurement System) from 2 to 380 K, in applied magnetic field ($H$) up to 70 kOe (along a [111] direction). Transport and magnetotransport measurements were typically performed in a Quantum Design Inc. Physical Property Measurement System from 2 to 300 K, in $H$ up to 90 kOe [again along a [111] direction, perpendicular to the plane of the crystals (and thus the current)]. Additional measurements were made in a closed-cycle refrigerator in a 10-kOe electromagnet. Soldered In contacts were employed, in a van der Pauw configuration, using DC excitation. As emphasized further below, such measurements were made in two distinct modes. In the first, contacts were applied to a pristine, as-grown surface, polishing to reduce the crystal thickness being done on only the back (noncontacted) side. All polishing used SiC paper, followed by 3- and 1-$\mu$m diamond slurries. In the second mode, both sides of the crystal were polished prior to contacting, meaning that contacts were placed on a prepolished surface. As will be seen below, these two contacting schemes produce very different results due to the sensitivity of the conduction to surface preparation. It is important to note that due to this surface conduction, when $\rho$ values are plotted and discussed in this work these are *apparent* resistivities, computed from the measured sheet resistances using the full crystal thickness.

## III. RESULTS AND ANALYSIS

### A. Structural and chemical characterization

Shown first in Fig. 1 is a summary of structural and chemical characterization data from representative $NiS_2$ crystals

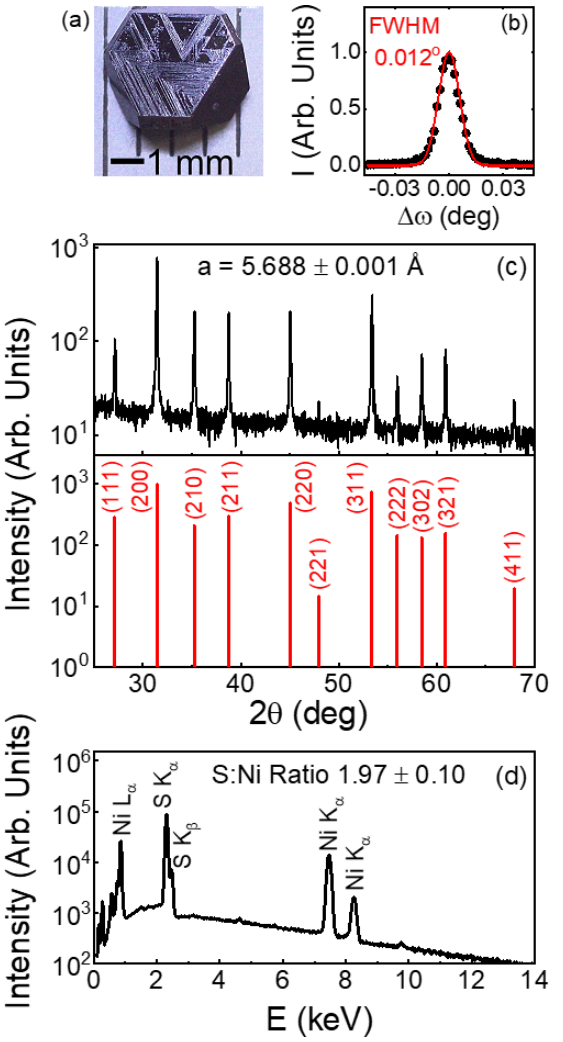


FIG. 1. (a) Photograph of a representative $NiS_2$ single crystal with a 1-mm scale bar. (b) 111 x-ray rocking curve of a typical $NiS_2$ single crystal, with the FWHM shown. (c) Wide-angle x-ray diffraction pattern from a representative ground $NiS_2$ crystal, with the expected pattern shown below. The deduced lattice parameter (from the sample height offset correction method) is shown, the error being from the associated fit. (d) Representative energy-dispersive x-ray spectrum from a $NiS_2$ single crystal, with the primary peaks labeled. The deduced S:Ni ratio of 1.97 ± 0.10 (systematic-error dominated) is shown. The two most prominent unlabeled low-energy peaks are from (surface) C and O.

from this study. From Fig. 1(a), as in $FeS_2$ [31,33,35,40] and $CoS_2$ [43], the crystal habit can be seen to provide clear indication of the crystallographic orientation, this six-sided crystal having (111) orientation based on XRD. The typical crystal sizes (several millimeters) are also comparable to CVT-grown $FeS_2$ [31,33,35,40] and $CoS_2$ [43], although surface roughness and faceting [clearly visible in Fig. 1(a)] are more pronounced in $NiS_2$. An important indicator of overall crystalline quality is shown in Fig. 1(b), where the typical full width at half maximum (FWHM) of the 111 high-resolution XRD rocking curve is seen to be ~0.01°. This is low on an absolute scale, and comparable to that in CVT-grown $FeS_2$ [31,33,35,40], establishing very low mosaic spread. The wide-

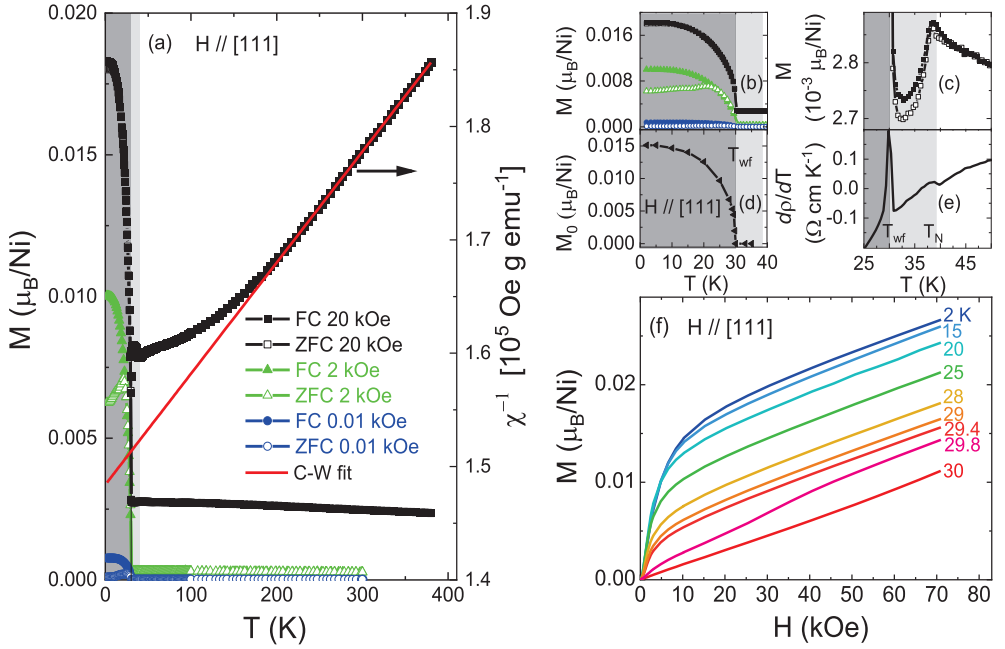


FIG. 2. (a) Temperature ($T$) dependence of the FC and ZFC magnetization ($M$) measured in 10-Oe (blue), 2-kOe (green), and 20-kOe (black) applied fields ($H$) along a [111] direction. FC and ZFC are shown as solid and open points, respectively. Plotted on the right axis are the 20-kOe data as inverse susceptibility ($\chi^{-1} = H/M$), along with a corresponding C-W fit (red line) between 200 and 380 K. As in panels (b)–(e), the dark and light gray regions correspond to the weak ferromagnetic and antiferromagnetic regions, respectively. (b)–(e) Low-temperature region $T$ dependence of: (b) $M$ in 10 Oe (blue), 2 kOe (green), and 20 kOe (black) [this is a close-up of the low-$T$ behavior in (a)]; (c) $M$ in 20 kOe; (d) $M_0$ as defined in (f); and (e) the $T$ derivative of the apparent resistivity ($\rho$). The Néel temperature ($T_N$) and onset temperature for weak ferromagnetism ($T_{wf}$) are shown. (f) $M(H)$ at various $T$ between 30 and 2 K; these are magnetizing curves starting at $H = 0$ after ZFC to the shown $T$ then warming above $T_N$ before repeating. Linear extrapolation of the high-$H$ (>40 kOe) curves to $H = 0$ defines the $M_0$ plotted in (d).

angle XRD pattern of a typical powdered crystal is presented in Fig. 1(c), showing only the expected reflections from $NiS_2$ [illustrated in red at the bottom of panel (c)], establishing the single-phase nature of these crystals. The extracted lattice parameter is 5.688 ± 0.001 Å, in very close agreement with prior work (e.g., Refs. [2,3,14]). Consistent with these findings, a typical EDS spectrum [Fig. 1(d)] reveals only Ni and S peaks (aside from the usual C and O surface contamination), the extracted S:Ni ratio being 1.97 ± 0.10, i.e., stoichiometric within the systematic error of EDS. As in $FeS_2$, this does not, of course, rule out nonstoichiometry-accommodating point defects (e.g., S vacancies) at the very low concentrations relevant to semiconductor doping [33].

### B. Magnetic properties

The magnetic properties of these crystals are summarized in Fig. 2. Shown first in Fig. 2(a) are magnetization ($M$) vs $T$ data taken after field cooling (FC, solid points) and zero-field cooling (ZFC, open points) in $H$ of 10 Oe, 2 kOe, and 20 kOe (blue, green, and black, respectively). As for all magnetometry in this work, $H$ was applied along a [111] direction, i.e., normal to the surface in Fig. 1(a). After a slow rise with decreasing $T$, $M$(T) reveals a clear transition at 30.0 K, where the FC $M$ rapidly increases and the low-$H$ FC and ZFC curves bifurcate. This marks $T_{wf}$, the overall behavior being in close agreement with prior work [3,4,11,12,14,15,19,20]. This behavior is more clearly illustrated in Fig. 2(b), which is a low-$T$ (< 40 K) blow-up of Fig. 2(a). The onset of weak ferromagnetism is clearly evident, the previously reported thermal hysteresis (which is only ∼0.1 K [12]) not being visible on this scale. The onset of AFM order at $T_N$ can be seen more clearly in Fig. 2(c), where $M(T)$ in 20 kOe is shown in close-up in the vicinity of $T_N$ and $T_{wf}$. A $T_N$ of 38.7 K is deduced from the peak in $M(T)$, in reasonable agreement with prior work [3,4,11,12,14,15,19,20]. Reported literature values for $T_N$ and $T_{wf}$ in fact vary slightly, in the ranges 37.0–39.3 K and 29.8–30.6 K [3,4,11,12,14,15,19,20], potentially related to uncontrolled deviations from ideal stoichiometry. Shown on the right axis of Fig. 2(a) are the 20-kOe $M(T)$ data converted to inverse susceptibility ($H/M$), along with a C-W fit. The linear region between 380 and ∼200 K yields $\theta_{CW} = -1500$ K, and thus $|\theta_{CW}|/T_N \approx 39$. The corresponding effective number of Bohr magnetons is 3.2 $\mu_B$, not far from the spin-only theoretical value of 2.8 $\mu_B$. These values are in reasonable agreement with prior work (e.g., Refs. [15,19]), although it should be emphasized that the frustration ratio and effective number of Bohr magnetons varied somewhat from crystal to crystal, between 21–39 and 2.3–3.2 $\mu_B$, respectively. In all cases, a clear break from C-W behavior was observed below ∼200 K.

Complementary to the above, Fig. 2(f) displays $M(H)$ at various $T$. These data were taken after ZFC to each $T$, measuring $M(H)$ on magnetizing, and then warming above $T_N$ and repeating. $M(H)$ evolves from near-ideal paramagnetic behavior at 30 K (i.e., linearity), to weak FM behavior at the lowest

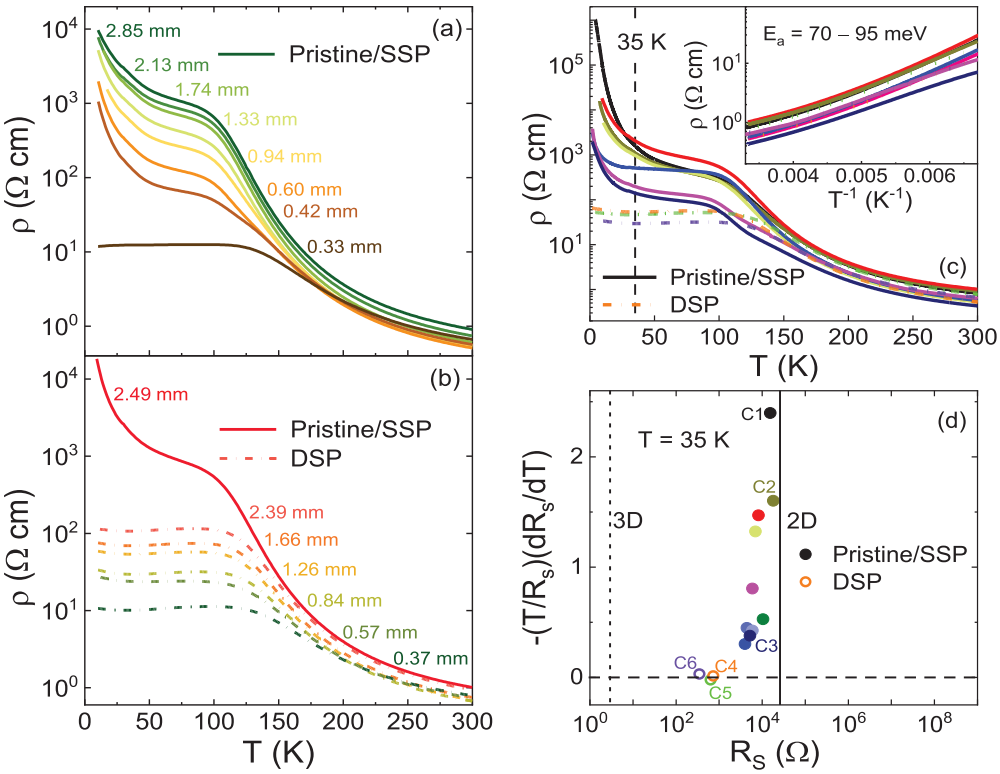


FIG. 3. (a) Temperature ($T$) dependence of the apparent resistivity ($\rho$) of an initially pristine single crystal, SSP from the back to reduce the thickness to the values shown (from 2.85 to 0.33 mm). (b) $T$ dependence of $\rho$ for an initially pristine single crystal, DSP to reduce the thickness to the values shown (from 2.49 to 0.37 mm). (c) $\rho(T)$ of multiple single crystals, with pristine/SSP in solid and DSP in dotted-dashed. Inset: $\rho$ ($\log_{10}$ scale) vs $T^{-1}$ in the high-$T$ region of (c) (150–300 K). Linear (i.e., Arrhenius) fits produce the shown range of activation energies ($E_A$). (d) 35 K value of $\frac{-T}{R_s}\frac{dR_s}{dT}$ vs $R_s$, where $R_s$ is the sheet resistance, for all crystals shown in (c) [35 K is marked on (c) for reference]. Solid symbols correspond to pristine/SSP, open symbols to DSP. The vertical solid and dotted lines correspond to the expected positions of 2D and 3D insulator-metal transitions, respectively, as discussed in the text. The labels "C1" through "C6" are for six crystals highlighted in further detail in later figures.

$T$, via an intermediate regime just below $T_{wf}$ (e.g., 29.8 K) with the previously observed slope change at intermediate $H$ (25–35 kOe at 29.8 K) [12,14]. The latter essentially marks a metamagnetic transition between AFM and weak FM order. The FM magnetization obtained by extrapolating the high $H$ (>40 kOe) $M(H)$ to $H = 0$, which we denote $M_0$, is then shown in Fig. 2(d), exhibiting very similar behavior to the high $H$ $M(T)$ in Fig. 2(b).

In general, the above observations establish that the magnetic properties of these $NiS_2$ single crystals are in very good agreement with prior studies [3,4,11,12,14,15,19,20]. We note as an aside that attempts to identify some of the most unusual features of this magnetism [specifically the non–C-W $M(T)$ at $T > T_N$ [14] and the weak FM behavior] as potential surface effects were unsuccessful. Unlike the transport properties discussed below, systematic thickness dependencies suggestive of surface effects could not be readily established for any of the anomalous magnetic parameters.

### C. Transport properties: Evidence for surface conduction

Measurements of $\rho(T)$ yield more interesting findings. Figure 3(a), for example, shows measurements of an initially pristine, as-grown crystal (topmost dark green curve), polished from its initial thickness ($t$) of 2.85 mm down to 0.33 mm, in successive steps. This was done in a mode where contacts were first placed on the pristine top surface, followed by progressive polishing from the back side. We refer to such crystals as "pristine/SSP," meaning a pristine top surface, single-side polished from the back to the stated $t$. The pristine $\rho(T)$ in Fig. 3(a) ($t = 2.85$ mm) exhibits the expected growth on cooling to ~100 K (i.e., insulating behavior), below which an abrupt break occurs, to significantly weaker $T$ dependence. Such data are immediately reminiscent of those of Thio and Bennett (see Sec. I) [13] and those recently obtained on $FeS_2$ [30,31], suggesting surface conduction where a more conductive surface layer shunts the excitation current at low $T$ as the less conductive Mott-insulating interior freezes out. The systematic $t$ dependence in Fig. 3(a), which was not probed in prior work [13], provides strong support for this conclusion. The weak $t$ dependence at 300 K becomes strong below 100–150 K, a reduction in $t$ from 2.85 to 0.42 mm, i.e., by a factor of ~7, inducing a similar, approximately tenfold decrease in $\rho$. This indicates sheet resistance ($R_s$) essentially independent of $t$ at low $T$, strong evidence of surface-dominated conduction [13,30,31].

Interestingly, reducing $t$ slightly further, from 0.42 to 0.33 mm, results in an abrupt change in $\rho(T)$ in Fig. 3(a). The low-$T$ $\rho$ drops significantly and the $T$ dependence becomes strongly suppressed, the $T \to 0$ value of $d\rho/dT$ crossing

from clearly negative (insulatinglike) to positive (metalliclike) at $t = 0.33$ mm. The origin of this behavior is clarified by Fig. 3(b), where equivalent $t$-dependent $\rho(T)$ data are shown for double-side polished (DSP) crystals, i.e., where an initially pristine crystal is double-side polished to the progressively lower $t$ shown in the figure. Polishing of the top, contacted surface is seen to immediately induce substantially decreased $\rho$ and flat $\rho(T)$ [compare $t = 2.49$ and 2.39 mm in Fig. 3(b)], $d\rho/dT$ becoming positive at intermediate $T$ before crossing to slightly negative at the lowest $T$. Further polishing to lower $t$ induces steady additional decreases in the apparent $\rho$. As in Fig. 3(a), the prominent $t$ scaling of $\rho$ is suppressed above 100–150 K, where $\rho(T)$ returns to the essentially $t$-independent insulating behavior reflective of the bulk. Comparison of Figs. 3(a) and 3(b) thus indicates that the nature of the surface conduction in $NiS_2$ crystals depends strongly on surface preparation. While all surfaces are more conductive than the Mott-insulating interior at low $T$, pristine surfaces of as-grown CVT crystals exhibit clearly negative (insulatinglike) $d\rho/dT$ as $T \to 0$ [e.g., the $t = 2.85$- and 2.49-mm cases in Figs. 3(a) and 3(b)], while polished surfaces are distinctly more conductive, with much flatter $\rho(T)$. In this light, the lowest $t$ data in Fig. 3(a) can then be simply interpreted in terms of the majority of the excitation current switching (via the crystal side surfaces) from the more resistive pristine top surface to the less resistive polished bottom surface below some threshold $t$, as would be expected in slab crystals with top contacts.

The substantial differences between as-grown and polished surface transport behaviors is further reinforced in Fig. 3(c), where multiple pristine crystals (solid lines) are compared to multiple DSP crystals (dotted-dashed lines). While some sample-to-sample variability occurs, as in $FeS_2$ [31], and as might be expected for such a surface-sensitive phenomenon, the as-grown crystals all exhibit flattening of $\rho(T)$ below ~100 K, followed by rapid rises in $\rho$ below ~50 K. DSP crystals, on the other hand, are all similar, exhibiting much flatter $\rho(T)$ below 100 K, where positive $d\rho/dT$ at intermediate $T$ gives way to weak negative $d\rho/dT$ below ~30 K. The bulk-dominated behavior above ~150 K is quite consistent among all crystals, however (pristine and DSP), as expected. As shown in the inset to Fig. 3(c), Arrhenius behavior is roughly adhered to in this regime (150–300 K), the extracted activation energies, $E_a$, falling between 70 and 95 meV, in reasonable agreement with prior work (see Sec. I) [15,19,21].

Further analysis of the low-$T$ (surface-dominated) $\rho(T)$ in the main panel of Fig. 3(c) is shown in Fig. 3(d), which plots, at a representative $T$ of 35 K, $\frac{-T}{R_s}\frac{dR_s}{dT}$ vs $R_s$. This is essentially a dimensionless temperature coefficient of sheet resistance as a function of the sheet resistance itself, as recently applied in surface conduction analysis of $FeS_2$ [31]. The various crystals in Fig. 3(c) present remarkably systematic behavior in Fig. 3(d), displaying a rapid rise in temperature coefficient of resistance as $R_s$ increases, signaling a surface IMT. As illustrated by the solid vertical line in Fig. 3(d), this IMT occurs close to the quantum resistance $h/e^2 \approx 26\,\mathrm{k\Omega}$ at which a strictly 2D IMT would be expected, and far from the $R_s$ at which a 3D IMT would be expected to occur. (The latter was estimated from the Mott minimum metallic conductivity

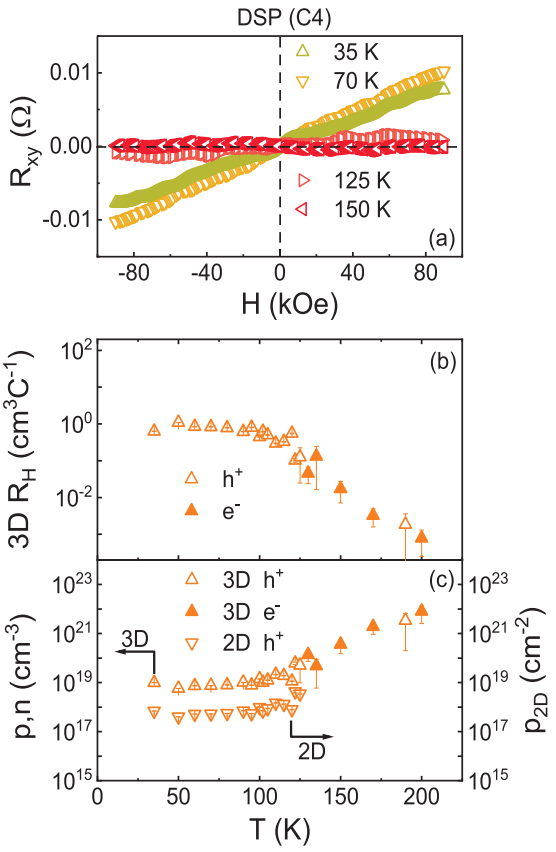


FIG. 4. (a) Applied magnetic field ($H$) dependence of the Hall resistance ($R_{xy}$) of a DSP single crystal (C4) at 35, 70, 125, and 150 K. (b) Temperature ($T$) dependence of the Hall coefficient ($R_H$), extracted assuming 3D conduction throughout the entire crystal thickness (0.70 mm). As in (c), solid symbols represent electronlike Hall signals, open symbols holelike Hall signals. (c) $T$ dependence of the hole or electron density ($p$ or $n$, respectively). "3D" values (left axis) assume conduction throughout the entire crystal thickness (0.70 mm), while "2D" values (right axis) assume purely 2D transport in the surface-dominated regime (i.e., below ~115 K).

[44] with an approximate generic $t$ of 0.1 mm, yielding the dotted vertical line.) Significantly, however, in prior work on $FeS_2$ crystals this correlation was even clearer, $\frac{-T}{R_s}\frac{dR_s}{dT}$ turning sharply upwards at exactly 26 kΩ [31]. In $NiS_2$, the upturn in $\frac{-T}{R_s}\frac{dR_s}{dT}$ is shifted distinctly below 26 kΩ, towards the 3D line. The pristine crystals in Fig. 3(d) (solid points) in fact lie close to the 2D IMT line, while the DSP crystals (open points) reach $R_s$ values well below $h/e^2 \approx 26\,\mathrm{k\Omega}$, suggesting that polished $NiS_2$ surfaces exhibit transport that is more 3D in nature.

That DSP crystals indeed exhibit 3D surface conduction rather than truly 2D surface conduction is strongly supported by Hall effect data. As for the remainder of this paper, some representative crystals are labeled in Fig. 3(d), with C1, C2, C3 denoting pristine crystals, and C4, C5, C6 denoting DSP crystals; this labeling is in order of decreasing $R_s$ [see Fig. 3(d)]. While Hall effect measurements on pristine crystals were found to be very challenging, particularly in the low-$T$, high-$R_s$ regime, as illustrated in Fig. 4 using C4 as a representative example, DSP crystals present more easily measurable Hall signals. Importantly, Fig. 4(a) illustrates that

Hall resistance ($R_{xy}$) vs perpendicular $H$ data reveal only small Hall effect at high $T$ (e.g., 150 and 125 K), in the bulk-dominated regime, but a much larger Hall effect at low $T$ (e.g., 70 and 35 K), in the surface-dominated regime. The $T$ dependence of the Hall coefficient ($R_H$) extracted from such data [from simple linear fitting to $R_{xy}(H)$] is shown in Fig. 4(b), solid points indicating negative (i.e., electronlike) $R_H$ and open points positive (i.e., holelike) $R_H$. Importantly, these $R_H$ values are extracted under the assumption of 3D bulk conduction, i.e., using the entire crystal thickness (0.70 mm). The $R_H$ in the bulk-dominated high-$T$ regime is seen to be low and negative, such Hall behavior being nontrivial to interpret in Mott insulators. $R_H$ grows on cooling, however, becoming larger and *positive* (i.e., holelike) below this crystal's bulk-to-surface crossover at ∼115 K, likely indicating a $p$-type surface, as in $FeS_2$, and as found by Thio and Bennett [13]. As in the 125 K data in Fig. 4(a), some evidence for nonlinearity in $R_{xy}(H)$ emerges in the crossover region, although this is obscured by the low magnitude of $R_H$ in the bulk-dominated high-$T$ regime. This is in contrast to $FeS_2$ crystals, where both the $n$-type bulk and $p$-type surface have sufficient mobility to enable tracking of nonlinear $R_{xy}(H)$ across the bulk-to-surface $n$-to-$p$ crossover [31]. Below ∼115 K, $R_H$ in Fig. 4(b) is then approximately $T$ independent down to 35 K.

While these data are again reminiscent of those of Thio and Bennett [13], quantitative analysis highlights important differences. As shown on the right axis of Fig. 4(c), for example, analyzing the $R_H(T)$ values from Fig. 4(b) in terms of purely 2D surface conduction results in surface hole densities ($p_{2D}$) over $10^{17}$ cm$^{-2}$ between 35 and 100 K. This is approximately three orders of magnitude above the $p_{2D}$ reported by Thio and Bennett [13] ($5 \times 10^{14}$ cm$^{-2}$), and indeed far above the Ni ion areal density, rendering it unphysical. The surface conduction in this regime is thus clearly not purely 2D. At the other extreme, analyzing the data of Fig. 4(b) assuming 3D transport throughout the entire thickness results in the 3D densities shown on the left axis of Fig. 4(c), giving $p \approx 10^{19}$ cm$^{-3}$ between 100 and 35 K. The true situation is undoubtedly between these extremes. Assuming a 3D hole density on the order of the volumetric Ni ion density (analogous to the 2D case of Thio and Bennett [13]), for example, yields a conductive layer thickness of the order of 100 nm, providing a rough estimate of the surface layer thickness in the DSP case. Consistent with the inference from Fig. 3(d), we thus conclude that polishing $NiS_2$ crystal surfaces not only decreases $R_s$ to far below $h/e^2 = 26\,\text{k}\Omega$, and induces strikingly flat $\rho(T)$, but also results in Hall densities that are only interpretable in terms of 3D, not 2D, transport. All indications thus suggest that while our pristine as-grown $NiS_2$ surfaces exhibit close to 2D insulating transport as $T \to 0$, polished surfaces enter a 3D surface conduction regime with metallic behavior. In essence, the effective thickness of the surface conduction layer appears to increase significantly with polishing.

The above deductions are yet further solidified by additional quantitative analysis of the form of $R_s(T)$ in pristine and DSP crystals. Figure 5(a), for example, plots $R_s$ on a $\log_{10}$ scale vs $T^{-1/2}$ for the pristine crystals C1, C2, and C3, probing for behavior of the form

$$R_s(T) = R_{s,0}\exp(T_0/T)^{1/2}, \tag{1}$$

where $R_{s,0}$ and $T_0$ are constants. This is the characteristic form of Efros-Shklovskii variable-range hopping (ES VRH) [45], which Fig. 5(a) illustrates is closely followed at low $T$ in crystals C1, C2, and C3. This is further supported by Zabrodskii analysis, which yields an exponent of 1/2 as opposed to alternative possibilities, as in $FeS_2$ [31]. Equation (1) in fact provides a good description of the data over as much as two orders of magnitude in $R_s$, the only obvious deviation being the small but distinct anomaly at $T_{wf}$ [vertical dashed line in Fig. 5(a)], which we return to below. We thus conclude that ES VRH is the active low-$T$ transport mechanism in the surface layer of our as-grown $NiS_2$ crystals, the extracted $T_0$ decreasing from 700 to 183 to 60 K from C1 to C2 to C3, i.e., as a surface IMT is approached. Further supporting this conclusion, Figs. 5(b)–5(d) show low-$T$ (35 K) MR data on crystals C1, C2, and C3, plotted as $\ln[R_s(H)/R_s(0)]$ vs $H$, probing for behavior of the form

$$\ln\left(\frac{R_s}{R_s(0)}\right) = \frac{s}{\hbar^2}L_c^4H^2\left(\frac{T_0}{T}\right)^{3/2}, \tag{2}$$

where $s = 0.0015$ and $L_c$ is the localization length. This is the expected form of the positive MR in ES VRH, which arises due to field-induced diamagnetic wave-function shrinkage [45]. As shown in Figs. 5(b)–5(d), Eq. (2) (solid red lines) describes the data reasonably well, the $T_0$ values determined from the analysis in Fig. 5(a) then enabling extraction of $L_c$ from the MR fits, yielding 3, 5, and 8 nm for C1, C2, and C3, respectively. As expected, $L_c$ grows with decreasing low-$T$ $R_s$, as a surface IMT is approached. Two additional conclusions can be drawn from this analysis. First, both the $T$ and $H$ dependence are consistent with ES VRH, strongly supporting ES VRH over any alternative forms of hopping. Second, with $T_0$ and $L_c$ values known, $T$-dependent average hopping lengths can be extracted [45], yielding, at 35 K, hopping lengths close to 3 nm in all cases. Truly 2D ES VRH would require the conductive surface layer thickness to be of this order, meaning that the surface layer thickness in the SSP case can be constrained down to at least ∼3 nm, quite similar to $FeS_2$ [31].

Figure 5(e) shows the same data as Fig. 5(a), this time plotted as sheet conductance, $G_s$ vs $T$ (along with the ES VRH fits). Also shown in Fig. 5(e) are the $G_s(T)$ data for the DSP crystals C4, C5, and C6, which, consistent with Fig. 3, exhibit much larger $G_s$, and weaker $T$ dependence, due to their 3D surface transport. As illustrated by the solid red line fits, $G_s(T)$ in these DSP crystals is well described by 3D electron-electron interaction and weak localization (WL) corrections, i.e.,

$$G_s(T) = G_s(0) + mT^{1/2} + BT^{p/2}. \tag{3}$$

The first term here is simply the $T \to 0$ value of $G_s$, while the second and third capture quantum corrections due to electron-electron interaction effects in the presence of disorder and WL, respectively [44,46]. The parameters $m$ and $B$ are then doping-dependent constants describing the strength of interaction and WL effects, while the exponent $p$ is the $T$ exponent of the electron dephasing time [46]. Initial fitting attempts immediately established $p \approx 3$ in these crystals, indicating dephasing limited by electron-phonon scattering [46], and $p$ was thus fixed at 3, leaving only $G_s(0)$, $m$, and $B$ as free parameters. The resulting magnitudes of $m$ and $B$ cluster

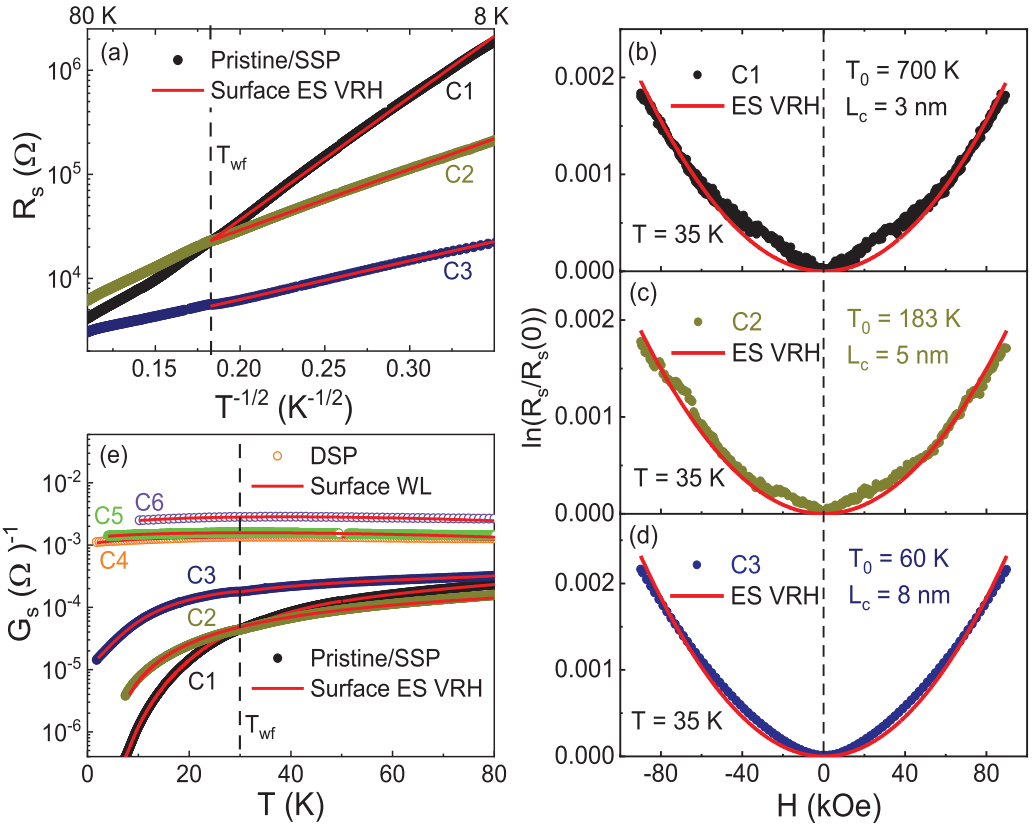


FIG. 5. (a) Sheet resistance ($R_s$) vs $T^{-1/2}$ for three pristine/SSP crystals (C1, C2, and C3); the solid red lines are straight-line fits, i.e., to Efros-Shklovskii variable-range hopping. (b)–(d) Applied magnetic field ($H$) dependence of $\ln[R_s/R(0)]$, where $R_s$ is the sheet resistance and $R_s(0)$ is its $H = 0$ value, for (c) crystal C1, (d) crystal C2, and (e) crystal C3, all at 35 K. The solid red lines are fits to the Efros-Shklovskii hopping model described in the text, resulting in the shown parameters. (e) Sheet conductance ($G_s$) vs $T$ for the pristine/SSP crystals C1, C2, and C3, in addition to DSP crystals C4, C5, and C6. The red solid lines through the C1, C2, and C3 data are identical to those in (a) (i.e., Efros-Shklovskii fits). The red solid lines through the C4, C5, and C6 data are to the 3D weak localization model described in the text. In both (a) and (e) the onset temperature of weak ferromagnetism ($T_{wf}$) is indicated.

around $\sim 2 \times 10^{-4}\Omega^{-1}\,\mathrm{K}^{-1/2}$ and $\sim 2 \times 10^{-6}\Omega^{-1}\,\mathrm{K}^{-3/2}$, respectively, but with opposite signs, indicating that the weak maximum in $G_s(T)$ in Fig. 5(e) [i.e., the minimum in $\rho$ in Figs. 3(b) and 3(c)] arises due to competition between these terms [46].

Significantly, with the bulk $R_s$ established to be of the form $R_s(T) = R_{s,0}\exp(E_a/k_BT)$ [Fig. 3(c), inset], and the surface $R_s$ known to be described by ES VRH in pristine crystals [i.e., $R_s(T) = R_{s,0}\exp(T_0/T)^{1/2}$] or 3D electron-electron interaction/WL in polished crystals [i.e., $G_s(T) = G_s(0) + mT^{1/2} + BT^{3/2}$], a two-channel conduction model can be used to describe $R_s(T)$ at *all* $T$. A simple parallel resistor model was used for this purpose, all necessary parameters being fixed from low-$T$ surface-dominated fits [Figs. 5(a) and 5(e)] and high-$T$ bulk-dominated fits [Fig. 3(c), inset]. As can be seen from Figs. 6(a) and 6(c), where crystals C1 and C4 are shown as representative of the pristine and DSP cases, respectively, this procedure works reassuringly well. The solid red lines (two-channel model) capture the bulk-to-surface crossover reasonably well in both cases, the green and blue dashed lines showing the bulk and surface contributions, with their intersection point giving the crossover temperature. This crossover temperature is 109 and 115 K in these two crystals.

The remainder of our analysis focuses on MR, demonstrating that its $T$ evolution on warming above the 35 K illustrated in Figs. 5(b)–5(d) can also be understood in terms of the surface-to-bulk crossover. Before proceeding to this, however, we briefly return to the issue of interplay between transport and magnetism, the first indication of which is the anomaly at $T_{wf}$ in Fig. 5(a). While not readily apparent in Figs. 5(a) and 5(e), such anomalies at $T_{wf}$ not only occur in all crystals (both pristine and DSP), but are also accompanied by weaker anomalies at $T_N$. A representative crystal demonstrating this (C5) is highlighted in Fig. 2(e), where $d\rho/dT$ is plotted vs $T$, revealing the anomaly at $T_{wf}$ in addition to a weaker one at $T_N$, only readily discernible in DSP crystals. Such features, while not widely acknowledged, *have* been detected in some single-crystal transport measurements [18,19,21]. It remains a challenge to understand these anomalies in more detail, however, including their relative size at $T_{wf}$ and $T_N$. One important point we wish to emphasize in this regard is that, with surface conduction now understood to be entirely dominant in this 30–40 K range (which lies far beneath the surface-to-bulk crossover temperatures of any of our samples), it is *surface* (not bulk) transport that data of the type shown in Fig. 2(e) reveal are sensitive to magnetic order. The anomaly at $T_{wf}$

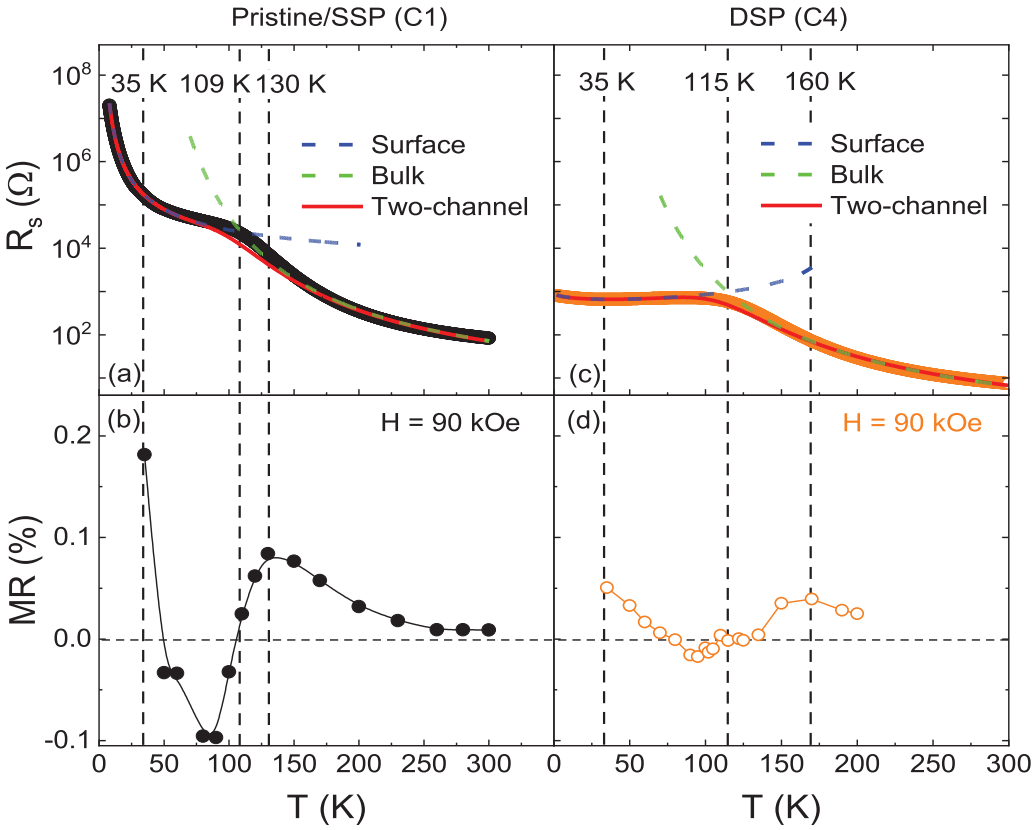


FIG. 6. Temperature ($T$) dependence of the sheet resistance ($R_s$) of (a) a pristine/SSP crystal (C1), and (c) a DSP crystal (C4). The lines through the data represent the surface, bulk, and two-channel model fits, as indicated. (b), (d) Corresponding $T$ dependence of the magnetoresistance ratio (in %) for (b) crystal C1 (pristine/SSP), and (d) crystal C4 (DSP). In (b), (d) the solid line is simply a guide to the eye. The vertical dashed black lines are at 35 K (the lower-temperature limit for the MR analysis), the surface-to-bulk crossover temperature (defined as the points where bulk and surface resistances cross), and the temperature at which surface contibutions become significant (where the positive MR begins to decrease).

being so much larger than the one at $T_N$ is then intriguing with respect to the possible scenario of the unexplained weak ferromagnetism being surface related. As noted in Sec. III B, however, initial attempts to correlate the weak FM magnetization with crystal thickness, for example, were not successful; further work along these lines would clearly be worthwhile.

### D. Magnetoresistance

Moving to the final issue of the $T$- and $H$ dependence of the MR in these $NiS_2$ single crystals, shown in Figs. 6(b) and 6(d) are 90-kOe MR($T$) data for representative crystals C1 (pristine) and C4 (DSP). The MR($T$) is seen to be closely correlated with $R_s(T)$ in both cases. Specifically, the MR in the high-$T$ bulk-dominated regime is small and positive, increasing on cooling. A maximum in the MR then emerges at lower $T$, as the bulk-to-surface crossover is approached. Very close to the crossover (109 K for C1 and 115 K for C4), the 90-kOe MR then inverts to negative, reaching a minimum at intermediate $T$ before rising rapidly to positive values at the lowest $T$ that could be probed. In essence, we argue that this apparently quite complex MR can be simply understood in terms of what we have already established regarding bulk and surface transport. As shown in Figs. 7(a) and 7(f), the $H$ dependence of the positive MR in the high-$T$ bulk-dominated regime is quadratic, indicative of the ordinary MR effect that would be expected in a semiconductor without magnetic order [31]. At the 110 K temperature in Figs. 7(b) and 7(g), as the bulk-to-surface crossover is approached, the MR then picks up a low-$H$ negative component, which dominates by 90 K [Figs. 7(c) and 7(h)], near the MR($T$) minima in Figs. 6(b) and 6(d). Further cooling to 50–70 K [Figs. 7(d) and 7(i)] then introduces a second high-field positive MR contribution, which becomes dominant at 35 K [Figs. 7(e) and 7(j)]. Simply, we ascribe the negative MR contribution at intermediate $T$, where surface transport first becomes dominant, to the WL already established by Fig. 5(e) in the DSP case, and which could be reasonably expected to precede the strong localization established in Figs. 5(a) and 5(e) in the pristine case. Importantly, we verified that the negative MR in, e.g., Fig. 7(c), is greatly suppressed for in-plane fields, consistent with WL, and counter to alternative possibilities such as isotropic spin-disorder related MR. We also note that on the basis of the low-$Z$ constituents (and thus weak spin-orbit interaction), WL would be expected over weak antilocalization in $NiS_2$. At lower $T$, as the strongly localized regime is entered [in the pristine case, Figs. 5(a)–5(d)], or approached (in the DSP case), positive MR then turns on, as established in the pristine case by the analysis of Figs. 5(b)–5(d) in terms of ES VRH [45]. The nonmonotonic 90-kOe MR($T$) in Figs. 6(b)

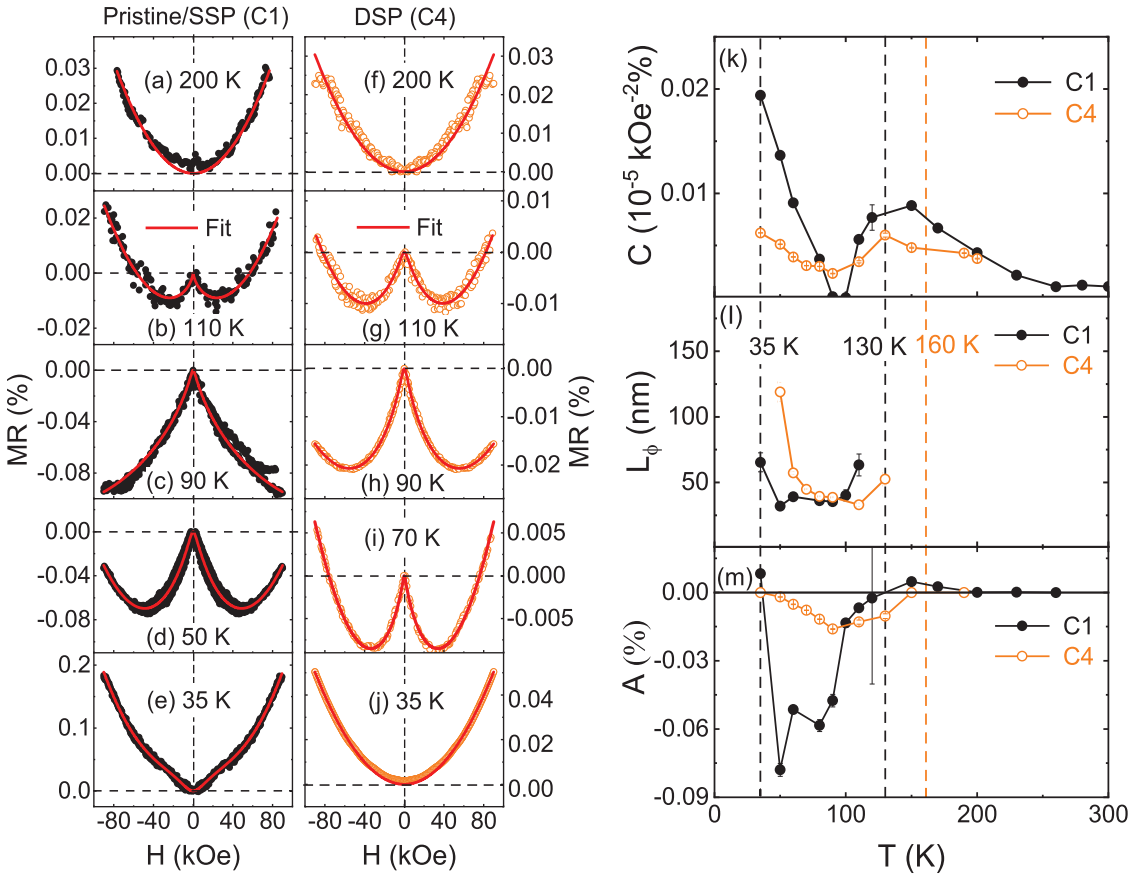


FIG. 7. Applied magnetic field ($H$) dependence of the MR ratio (in %) for a pristine/SSP crystal (C1) (a)–(e) and a DSP crystal (C4) (f)–(j) at temperatures of 200, 110, 90, 50/70, and 35 K (from top to bottom). The solid red line fits in each case are to the model described in the text. (k)–(m) Temperature ($T$) dependence of the parameters extracted from fits of the type shown in (a)–(j). (k), (l), and (m), show, respectively, the parameters $C$, $L_\phi$, and $A$, as defined in the text. The vertical dashed lines at 35, 130, and 160 K have the same meaning as in Fig. 6, i.e., the lower-$T$ limit of the MR analysis, and the points at which surface contributions dominate and emerge.

and 6(d) can thus be described as bulk-dominated ordinary positive MR at the highest $T$, crossing to surface-dominated negative MR associated with WL, then to positive MR due to strongly localized transport, again in the surface region.

Quantitative evidence for the above was obtained by fitting $T$-dependent MR($H$) data of the type shown in Figs. 7(a)–7(j) to the phenomenological form:

$$MR[\%] = A\left[\psi\left(\frac{1}{2}+\frac{H_\phi}{H}\right) - \ln\left(\frac{H_\phi}{H}\right)\right] + CH^2, \quad (4)$$

where $\psi$ is the digamma function, $H_\phi = h/8\pi L_\phi{}^2$, and $L_\phi$ is the electron phase decoherence length. The $CH^2$ term here, where $C > 0$, is used to describe the quadratic positive MR at high $T$ and the approximately quadratic positive MR at the lowest $T$ [Eq. (2) reduces to quadratic in the low-$H$, low-MR limit]. The other terms in Eq. (4) derive from the HLN (Hikami-Larkin-Nagaoka) formula describing WL-induced negative MR under the assumption of 2D conditions [46,47], with the prefactor $A$ simply describing the strength of the WL contribution relative to the positive MR components (parametrized by $C$). As shown by the red solid line fits in Figs. 7(a)–7(j), Eq. (4) provides a very good description of MR($T$,$H$) at all $H$ and $T$. We note at this point that the HLN formula strictly describes only 2D and quasi-2D situations, but fitting with the 3D equivalent [46,48], produced near-identical fit quality and parameters; this is understandable given the intermediate regime between 2D and 3D relevant here. The resulting fit parameters $C$, $A$, and $L_\phi$ are shown vs $T$ in Figs. 7(k)–7(m). As expected, the positive MR amplitude $C$ simply grows on cooling from high $T$ (reflecting the growth of ordinary MR), is barely nonzero at intermediate $T$ (where WL dominates), but grows rapidly at the lowest $T$ [where strong localization kicks in (in the pristine case), or is approached (in the DSP case)]. Correspondingly, in both pristine and DSP cases, non-negligible $A$ is required only in the intermediate-$T$ regime where surface WL is dominant [Fig. 7(m)]. $A$ is also largest in magnitude in crystal C1 (SSP), consistent with its higher resistance, closer to the quantum value; in C4 (DSP) the resistance falls far beneath the quantum value and $A$ is correspondingly smaller in magnitude, i.e., WL effects are weaker. The resulting $L_\phi$ values in the intermediate-$T$ regime, which dictate the shape of MR($H$) [Figs. 7(b)–7(d), 7(g)–7(i)], plateau at ∼30 nm in Fig. 7(l) before increasing on cooling. These absolute values are large but not entirely unreasonable in this $T$ range [49], the lack of a simple power-law increase on cooling likely being due to contamination by the positive MR effect at low $T$, i.e., imperfect separation of MR components by our analysis with Eq. (4). Overall, however, we conclude that Eq. (4) provides a

reasonable description of these MR data at all $T$ and $H$, quantitatively supporting the concept of ordinary positive MR in the high-$T$ bulk-dominated regime, crossing over to WL-induced negative MR in the surface-dominated intermediate-$T$ regime, and then positive MR associated with stronger localization in the surface-dominated lowest-$T$ regime.

## IV. SUMMARY AND CONCLUSIONS

Taken together, the data and analyses presented in Sec. III essentially establish that the $NiS_2$ crystals studied in this work are comparable to the highest structural/chemical quality $TMS_2$ crystals reported, that they exhibit magnetic properties very similar to prior work, and that they exhibit prominent surface conduction. The latter is unequivocal, supported by the characteristic form of the $T$ dependence of the apparent $\rho$, its conspicuous $t$ scaling at low $T$, the sensitivity of these effects to surface preparation, the close-to-2D nature of the transport, and the quantitative success of two-channel (bulk and surface) conduction modeling. This work also significantly advances the understanding of this surface conduction in $NiS_2$. The significant variability, from 2D ES VRH on pristine surfaces, to 3D weakly localized metallic transport on polished surfaces, casts much light, for example, on the scattered prior literature reports on $\rho(T)$ [13,15,16,19–23] and the resulting ambiguity over the true electronic ground state of $NiS_2$ [16]. Explicitly, the surface preparation and polishing procedures in these works were likely widely varied, thereby inadvertently inducing variable surface transport behaviors. Future work directed at understanding exactly how surface treatments such as polishing can induce such 3D transport would clearly be worthwhile. Depth profiling with photoemission spectroscopy (and other techniques) to track band bending and possible stoichiometry changes in pristine vs polished crystals could well address this issue. Figures 5–7 further establish that the MR behavior of $NiS_2$ follows directly from the conclusions regarding surface transport, progressing from positive ordinary MR in the high-$T$ bulk-dominated regime, to WL-related negative MR in the intermediate-$T$ surface-dominated regime, to reentrant positive MR in the more strongly localized lowest-$T$ regime.

These findings also have broader implications. First, with surface conduction recently established in single-crystal $FeS_2$ [30–33,35,37,40] (and hypothesized to derive from surface states that pin $E_F$ near the valence-band edge), with minority spin surface states known to exist in $CoS_2$ [41], and with the current work unequivocally establishing surface conduction in $NiS_2$, the question of generality naturally arises. We in fact hypothesize that surface states may be a universally important feature in $TMS_2$ compounds. Ligand field theory arguments by Bronold *et al.* have been widely referenced to rationalize in-gap (near valence-band) surface states in $FeS_2$ [36,38,39], and could be more generally applicable than previously thought, potentially supporting surface states in the (Mott physics-related) band gap of $NiS_2$, and the minority spin gap of $CoS_2$. There are also other commonalities among surface effects in $TMS_2$ compounds, including the $p$-type character of both the $NiS_2$ and $FeS_2$ surfaces, suggesting upward surface band bending in both cases. Clearly, future work along these lines would be valuable, including further analytical and computational theory of surface effects, studies attempting to connect surface spectroscopic and microscopic techniques with transport (including probing the depth-dependent surface band bending), studies attempting to elucidate a potential role for band-structure topology, and exploration of related phenomena in other $TMS_2$ compounds, e.g., $CuS_2$ and $ZnS_2$. With respect to topology, it is worth noting that a recent high-throughput computational study [50] identified $NiS_2$ as a possible magnetic topological material, although this may not survive the addition of the electronic correlations that are clearly essential to understand $NiS_2$. It should also be emphasized here that further understanding in these directions could have significant applied impact, as pyrite-structure $TMS_2$ compounds are being actively explored for various device applications, including photovoltaics, electrocatalysis, and battery electrodes [29–40,51]. These are heterostructured devices, obviously rendering the surface electronic behavior critical, as highlighted in the recent progress with $FeS_2$ [30–35,37,40].

Our findings also have clear implications for the understanding of the feature of $NiS_2$ that has motivated the majority of the fundamental research on this material: the transition from Mott insulator to metal vs pressure, Se substitution, electron-hole doping with Cu/Co, etc. [3,4,17,18,20,22–28]. What occurs in such systems is a strikingly rich progression in $\rho(T)$, often involving abrupt changes in slope at low $T$ [3,20,22,23]. In light of the results in this paper, it seems highly likely that at least some of these features are associated with surface conduction, which was not taken into account in the vast majority of such studies. While the *existence* of IMTs in these systems is in little doubt, the *positions* of these transitions (i.e., critical pressures, temperatures, and compositions), and their *systematics* vs composition, pressure, etc., have thus likely not been properly determined in many prior studies. We therefore believe it is imperative that we revisit and reexamine IMTs in these $NiS_2$-based materials, which are often touted as model systems for this type of physics.

## ACKNOWLEDGMENTS

Work supported primarily by the U.S. Department of Energy through the University of Minnesota Center for Quantum Materials under Grant No. DE-SC-0016371. S.E.-K. additionally acknowledges Faculty Research Grant No. 2020-M-S138 from the American University of Sharjah. Crystal growth and structural/chemical characterization supported partially by the National Science Foundation through the University of Minnesota MRSEC under Award No. DMR-2011401.

[1] H. S. Jarrett, W. H. Cloud, R. J. Bouchard, S. R. Butler, C. G. Frederick, and J. L. Gillson, Phys. Rev. Lett. **21**, 617 (1968).

[2] T. A. Bither, R. J. Bouchard, W. H. Cloud, P. C. Donohue, and W. J. Siemons, Inorg. Chem. **7**, 2208 (1968).

[3] S. Ogawa, S. Waki, and T. Teranishi, Int. J. Magn. **5**, 349 (1974).
[4] S. Ogawa, J. Appl. Phys. **50**, 2308 (1979).
[5] L. Wang, T. Y. Chen, and C. Leighton, Phys. Rev. B **69**, 094412 (2004).
[6] L. Wang, K. Umemoto, R. M. Wentzcovitch, T. Y. Chen, C. L. Chien, J. Checkelsky, J. Eckert, E. D. Dahlberg, and C. Leighton, Phys. Rev. Lett. **94**, 056602 (2005).
[7] L. Wang, T. Y. Chen, C. L. Chien, J. G. Checkelsky, J. Eckert, E. D. Dahlberg, K. Umemoto, R. M. Wentzcovitch, and C. Leighton, Phys. Rev. B **73**, 144402 (2006).
[8] C. Leighton, M. Manno, A. Cady, J. W. Freeland, L. Wang, K. Umemoto, R. M. Wentzcovitch, T. Y. Chen, C. L. Chien, P. L. Kuhns, M. J. R. Hoch, A. P. Reyes, W. G. Moulton, E. D. Dahlberg, J. Checkelsky, and J. Eckert, J. Phys.: Condens. Matter **19**, 315219 (2007).
[9] J. Walter, B. Voigt, E. Day-Roberts, T. Birol, R. Fernandes, and C. Leighton, Sci. Adv. **6**, eabb7721 (2020).
[10] R. L. Kautz, M. S. Dresselhaus, D. Adler, and A. Linz, Phys. Rev. B **6**, 2078 (1972).
[11] T. Miyadai, K. Takizawa, H. Nagata, H. Ito, S. Miyahara, and K. Hirakawa, J. Phys. Soc. Jpn. **38**, 115 (1975).
[12] K. Kikuchi, J. Phys. Soc. Jpn. **47**, 484 (1979).
[13] T. Thio and J. W. Bennett, Phys. Rev. B **50**, 10574 (1994).
[14] T. Thio, J. W. Bennett, and T. R. Thurston, Phys. Rev. B **52**, 3555 (1995).
[15] M. Matsuura, Y. Endoh, H. Hiraka, K. Yamada, A. S. Mishchenko, M. Nagaosa, and I. V. Solovyev, Phys. Rev. B **68**, 094409 (2003).
[16] D. D. Sarma, S. R. Krishnakumar, E. Wesschke, C. Schussler-Langeheine, C. Mazumdar, L. Kilian, G. Kaindl, K. Mamiya, S.-I. Fujimori, A. Fujimori, and T. Miyadai, Phys. Rev. B **67**, 155112 (2003).
[17] P. G. Niklowitz, P. L. Alireza, M. J. Steiner, G. G. Lonzarich, D. Braithwaite, G. Knebel, J. Flouquet, and J. A. Wilson, Phys. Rev. B **77**, 115135 (2008).
[18] Y. Feng, R. Jaramillo, A. Banerjee, J. M. Honig, and T. F. Rosenbaum, Phys. Rev. B **83**, 035106 (2011).
[19] T. Higo and S. Nakatsuji, J. Phys. Soc. Jpn. **84**, 053702 (2015).
[20] S. Yano, D. Louca, J. Yang, U. Chatterjee, D. E. Bugaris, D. Y. Chang, L. Peng, M. Grayson, and M. Kanatzidis, Phys. Rev. B **93**, 024409 (2016).
[21] C. Clark and S. Friedemann, J. Magn. Magn. Mater. **400**, 56 (2016).
[22] Y. Sekine, H. Takahashi, N. Mori, T. Matsumoto, and T. Kosaka, Physica B **237–238**, 148 (1997).
[23] J. M. Honig and J. Spalek, Chem. Mater. **10**, 2910 (1998).
[24] A. K. Mabatah, E. J. Yoffa, P. C. Eklund, M. S. Dresselhaus, and D. Adler, Phys. Rev. Lett. **39**, 494 (1977).
[25] A. K. Mabatah, E. J. Yoffa, P. C. Eklund, M. S. Dresselhaus, and D. Adler, Phys. Rev. B **21**, 1676 (1980).
[26] P. Kwizera, A. K. Mabatah, M. S. Dresselhaus, and D. Adler, Phys. Rev. B **24**, 2972 (1981).
[27] P. Kwizera, M. S. Dresselhaus, and D. Adler, Phys. Rev. B **21**, 2328 (1980).
[28] A. Maignan, R. Daou, E. Guilmeau, D. Berthebaud, T. Barbier, O. Lebedev, and S. Herbert, Phys. Rev. Materials **3**, 115401 (2019).
[29] K. D. M. Rao, T. Bhuvana, B. Radha, N. Kurra, N. S. Vidhyadhiraja, and G. U. Kulkarni, J. Phys. Chem. C **115**, 10462 (2011).
[30] M. Limpinsel, N. Farhi, N. Berry, J. Lindemuth, C. L. Perkins, Q. Lin, and M. Law, Energy Environ. Sci. **7**, 1974 (2014).
[31] J. Walter, X. Zhang, B. Voigt, R. Hool, M. Manno, F. Mork, E. S. Aydil, and C. Leighton, Phys. Rev. Materials **1**, 065403 (2017).
[32] D. Liang, M. Cabán-Acevedo, N. S. Kaiser, and S. Jin, Nano Lett. **14**, 6754 (2014).
[33] B. Voigt, W. Moore, M. Manno, J. Walter, J. D. Jeremiason, E. S. Aydil, and C. Leighton, ACS Appl. Mater. Interfaces **11**, 15552 (2019).
[34] D. Ray, B. Voigt, M. Manno, C. Leighton, E. S. Aydil, and L. Gagliardi, Chem. Mater. **32**, 4820 (2020).
[35] B. Voigt, W. Moore, M. Maiti, J. Walter, B. Das, M. Manno, C. Leighton, and E. S. Aydil, ACS Mater. Lett. **2**, 861 (2020).
[36] A. Ennaoui, S. Fiechter, C. Pettenkofer, N. Alonso-Vante, K. Büker, M. Bronold, C. Höpfner, and H. Tributsch, Sol. Energy Mater. Sol. Cells **29**, 289 (1993).
[37] M. Cabán-Acevedo, N. S. Kaiser, C. R. English, D. Liang, B. J. Thompson, H. Chen, K. J. Czech, J. C. Wright, R. J. Hamers, and S. Jin, J. Am. Chem. Soc. **136**, 17163 (2014).
[38] M. Bronold, K. Buker, S. Kubala, C. Pettenkofer, and H. Tributsch, Phys. Status Solidi **135**, 231 (1993).
[39] M. Bronold, Y. Tomm, and W. Jaegermann, Surf. Sci. **314**, L931 (1994).
[40] B. Voigt, B. Das, D. M. Carr, D. Ray, M. Maiti, W. Moore, M. Manno, J. Walter, E. S. Aydil, and C. Leighton, Phys. Rev. Materials **5**, 025405 (2021).
[41] N. Wu, R. F. Sabirianov, W. N. Mei, Y. B. Losovyj, N. Lozova, M. Manno, C. Leighton, and P. A. Dowben, J. Phys.: Condens. Matter **21**, 295501 (2009).
[42] N. B. M. Schroter, I. Robredo, S. Klemenz, R. J. Kirby, J. A. Krieger, D. Pei, T. Yu, S. Stolz, T. Schmitt, P. Dudin, T. K. Kim, C. Cacho, A. Scnyder, A. Bergara, V. N. Strocov, F. de Juan, M. G. Vergniory, and L. M. Schoop, Sci. Adv. **6**, eabd5000 (2020).
[43] L. Wang, T. Y. Chen, C. L. Chien, and C. Leighton, Appl. Phys. Lett. **88**, 232509 (2006).
[44] N. Mott, *Metal-Insulator Transitions*, 2nd ed. (Taylor & Francis, London, 1990).
[45] B. I. Shklovskii and A. L. Efros, *Electronic Properties of Doped Semiconductors* (Springer, Berlin, 1984).
[46] P. A. Lee and T. V. Ramakrishnan, Rev. Mod. Phys. **57**, 287 (1985).
[47] S. Hikami, A. I. Larkin, and Y. Nagaoka, Prog. Theor. Phys. **63**, 707 (1980).
[48] A. Kawabata, Solid State Commun. **34**, 431 (1980); J. Phys. Soc. Jpn. **49**, 628 (1980).
[49] J. J. Lin and J. P. Bird, J. Phys.: Condens. Matter **14**, R501 (2002).
[50] Y. Xu, L. Elcoro, Z.-D. Song, B. J. Wieder, M. G. Vergniory, N. Regnault, Y. Chen, C. Felser, and B. A. Bernevig, Nature (London) **586**, 702 (2020).
[51] M. S. Faber, M. A. Lukowski, Q. Ding, N. S. Kaiser, and S. Jin, J. Phys. Chem. C **118**, 21347 (2014).